

MIT Open Access Articles

*Time limitations and geometrical parameters
in the design of microfluidic comparators*

The MIT Faculty has made this article openly available. **Please share** how this access benefits you. Your story matters.

Citation: Cartas-Ayala, Marco A., and Rohit Karnik. "Time Limitations and Geometrical Parameters in the Design of Microfluidic Comparators." *Microfluid Nanofluid* 17, no. 2 (December 11, 2013): 359–373.

As Published: <http://dx.doi.org/10.1007/s10404-013-1302-x>

Publisher: Springer Berlin Heidelberg

Persistent URL: <http://hdl.handle.net/1721.1/103104>

Version: Author's final manuscript: final author's manuscript post peer review, without publisher's formatting or copy editing

Terms of use: Creative Commons Attribution-Noncommercial-Share Alike



Time Limitations and Geometrical Parameters in the Design of Microfluidic Comparators

Marco A. Cartas-Ayala¹, Rohit Karnik*

77 Massachusetts Ave., Massachusetts Institute of Technology, Cambridge Ma., USA

[*karnik@mit.edu](mailto:karnik@mit.edu)

Phone: 617-324-1155

Abstract The ability to control the flow of particles (e.g. droplets and cells) in microfluidic environments can enable new methods for synthesis of biomaterials (Mann and Ozin 1996), bio characterization, and medical diagnosis (Pipper et al. 2007). Understanding the factors that affect the particle passage can improve the control over the particles' flow through microchannels (Vanapalli et al. 2009). The first step to understand the particle passage is to measure the resulting flow rate, induced pressure drop across the channel, and other parameters. Flow rates and pressure drops during passage of a particle through microchannels are typically measured using microfluidic comparators. Since the first microfluidic comparators were reported, a few design factors have been explored experimentally and theoretically, e.g. sensitivity (Vanapalli et al. 2007). Nevertheless there is still a gap in the understanding of the temporal and spatial resolution limits of microfluidic comparators. Here we explore, theoretically and experimentally, the factors that affect the spatial and temporal resolution. We determined that the comparator sensitivity is defined by the device geometry adjacent and upstream the measuring point in the comparator. Further, we determined that, in order of importance, the temporal resolution is limited by the convective time scale, capacitive time scale due to channel expansion, and unsteady time scale due to the flow inertia. Finally, we explored the flow velocity limits by characterizing the transition between low to moderate Reynolds numbers ($Re \ll 1$ to $Re \sim 50$). The present work can guide the design of microfluidic comparators and clarify the limits of this technique.

Keywords: *Lab-on-a-chip, droplets, cells, microfluidic manometer, mechanical properties, hydrodynamic resistance.*

1. Introduction

The flow and control of particles in microchannels has gained increased attention in recent years, in particular the case of droplets and cells. Droplets have numerous potential applications. Droplets can be used as vessels for small biological samples from single cells to small bacteria colonies (He et al. 2005); droplets can be used as micro-reactors in cases where chemicals are expensive (He et al. 2005). Controlling the formation of droplets in solution, i.e. emulsions, in highly controlled micro environments can potentially improve the production of diverse products ranging from shampoo to micro and nano particles for therapeutics (Xu et al. 2009). The analysis and control of biological samples at the cellular level can enable single cells analysis, a valuable tool for disease diagnosis and gene expression research. Further, the flow of cells in microchannels can enable devices with new functionalities. The passage time of cells through constricted microfluidic channels has been used to determine altered mechanical states of cells produced by diseases like cancer (softer cells) or malaria (stiffer cells).

As research progresses, the devices involving the passage of particles through microchannels have become more complex. The control of droplets and deformable particles has evolved from simple junctions regulated by pressure (Thorsen et al. 2001; Vestad et al. 2004) to complex fully integrated devices that use particles in logic microfluidic circuits that enable parallel and sequential analysis and processing. Parallel to the increment in device complexity, the need for models that can accurately predict the behavior of particles in the microchannels has increased. As a first step to create models for the passage of particles in microfluidic channels, it is necessary to measure and understand the factors that affect the particle passage, i.e. particle's size, particle's deformed geometry, particle's velocity, induced pressure drop across the microchannel, and variations in the total flow rate of the microchannel.

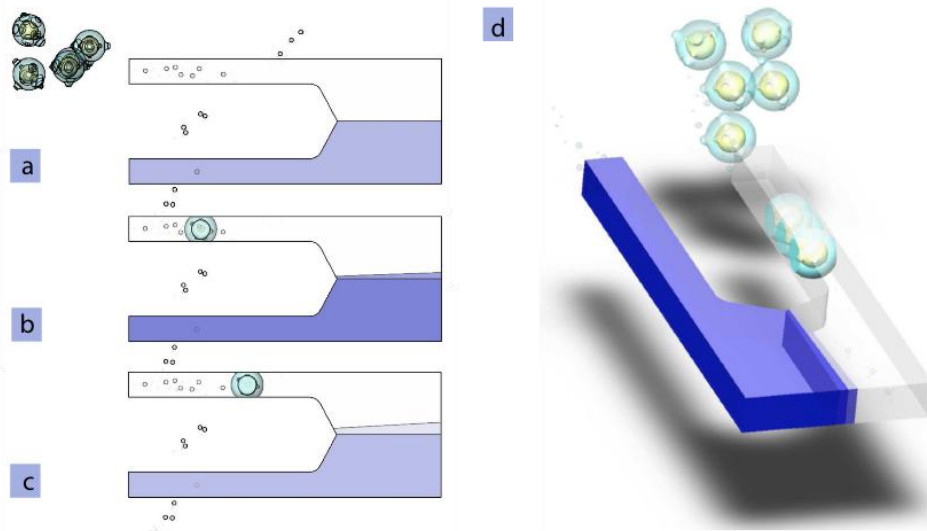


Figure 1. Microfluidic Differential Comparator. a-d) As a particle enters one of the two parallel channels, it modulates the flow through the channel, which causes a measurable deflection of the fluid interface indicative of the relative flow rates in the two channels.

While the particle's size, particle's deformed geometry, and particle's velocity can be measured with a simple camera recording the particle's passage; the induced pressure drop and variations in the total flow rate have to be measured indirectly using a microfluidic device known as a microfluidic comparator (**Fig. 1**). A microfluidic comparator is a device used to measure hydrodynamic variables in a microfluidic channel. Different implementations use different geometries but they share the sample principle: the movement of the interface created between a sample flow and a reference flow is used to measure relative flow rates.

A comparator consists of two identical channels, sample and reference channels, that merge into a third, measurement channel. Fluids of identical mechanical properties but different colour flow through the sample and reference channels. At the measuring channel both fluids merge forming a discernable interface. By measuring the movement of the fluid interface it is possible to obtain the relative flow fraction through the different liquid streams. Then, the relative flow rates are used to infer absolute flow rates, pressure drops, and induced resistances. Since microfluidic comparators can be used to extract flow rates and induced resistances, they can provide a measurement of the induced pressure drop at different parts of the microfluidic device, which ultimately can be translated into forces. Since microfluidic comparators can provide a complete picture of the physics involved in the passage of a particle through a microchannel, they are suitable to clarify the nature of the interactions between particles, microfluidic channels, and the resulting flows. As a consequence they constitute a valuable experimental tool to probe on the nature of particle-channel interactions.

The first microfluidic manometer (i.e. comparator) to measure pressure variations created by the passage of individual cells through microfluidic channels was reported in 2006 (Abkarian et al. 2006). Soon, alternate versions of the microfluidic manometer with enhanced sensitivity were used to measure resistance changes due to the passage of micro-droplets inside microfluidic channels (Vanapalli et al. 2009). Also in 2009, the induced hydrodynamic resistance was measured indirectly by analysing the flow patterns produced by droplets at bifurcations (Labrot et al. 2009; Sessoms et al. 2009). Abkarian and Vanapalli implementations differ in the geometry downstream of the measuring junction. In Abkarian's implementation, the measuring channel continues till the outlet port is reached (**Fig. 2**). On the other hand, in Vanapalli's implementation, the channel bifurcates into two identical outlet channels. Vanapalli's implementation was shown to be more sensitive than Abkarian's. The outlet channel bifurcation forces the fluid interface to have a larger deflection when a particle blocks the sensing channel. Nevertheless the increment of sensitivity comes at a price: the comparator interface is also sensitive to the passage of particles through the channels downstream of the measuring channel. Since in Abkarian's design the presence of particles downstream of the measuring junction does not disturb the measuring interface, we selected Abkarian's design for further study. Here, using Abkarian's design, we investigate the time limitations and relevant geometrical parameters in microfluidic comparators.

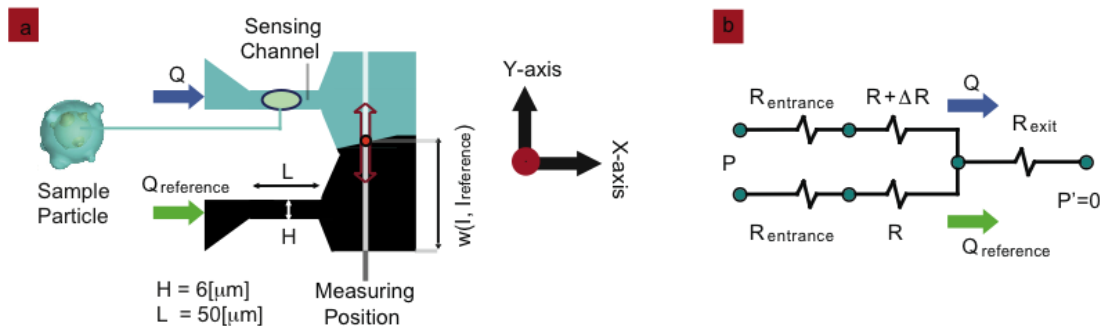


Figure 2. Microfluidic Differential Manometer. a) Schematic showing the basic design of a microfluidic differential manometer. b) Microfluidic differential manometer equivalent resistance circuit.

2. Materials and methods

2.1 Microfluidic manometer fabrication

Devices were fabricated by standard micromolding in polydimethylsiloxane (PDMS, Sylgard 184, Dow Corning) using a SU-8 photoresist mold (Microchem). The molds were placed in a large covered Petri dish containing several drops of perfluorooctyltrichlorosilane (10 min) to facilitate removal of PDMS. PDMS was mixed (10:1 ratio) and poured into the mold (4 mm layer), degassed, and baked (80 °C for 30 min). The PDMS was removed, perforated to form the channel inlets using a biopsy punch (0.5 mm internal diameter punch from Harris Uni-Core), and cleaned using isopropanol. Finally, the PDMS component containing the channels was bonded to a clean glass slide using air plasma (30 s, 500 mTorr) (Expanded Plasma Cleaner, Harrick Plasma, Ithaca, NY). The devices were connected to pressurized reservoirs containing the desired solutions via Tygon tubing, where the pressure was controlled using pressure regulators.

2.1 Microfluidic comparator geometry

Two different comparator geometries were used in this study, hereon referred as small and large cross-section devices. The small cross-section devices were used during the time delay characterization of the devices because they have smaller associated response time. The large cross-section devices were used during the interface displacement calibration experiments since they produce a larger video image with smaller relative error associated with the microscope resolution limits. The sensing and reference channels in the comparators used in this study have square cross sections. Square channels are used in the experiments because they can be manufactured consistently and readily with the same dimensions, and, since they are universally used in most microfluidic applications, the use of rectangular channels makes our measurements directly applicable to other systems. Further, square cross-section channels were used here to produce a more uniform deformation of the particles (compared to rectangular).

The small cross-section devices had sensing channels with square cross-sections of 6- μm side width (hence a hydrodynamic diameter, $D_H = 4 \frac{\text{Area}}{\text{Perimeter}}$, of 6 μm) and length of 50 μm . The small cross-section devices had inlet channels with a height of 6 μm , a width of 60 μm and a length of ~500 μm . The large cross-section devices had square cross-sections of 15- μm side width (hence a hydrodynamic diameter, $D_H = 4 \frac{\text{Area}}{\text{Perimeter}}$, of 15 μm) and length of 75 μm . In both types of devices, Tygon tubing with internal diameter of 500 μm and a length of 200 mm was used to connect the inlet channels to liquid reservoirs.

Images of the interface displacement as a function of time are shown in **Fig. 3**. From the images, the interface displacements at different positions in the measuring channel were extracted. As the particle enters the measuring channel, it gets compressed and starts to increase the hydrodynamic resistance. Once deformed, the particle enters the channel and the induced resistance reaches a steady maximum value. Finally, as the particle exits the channel, the induced resistance decreases to zero. It must be noted that any measurements of the induced resistance once the particle has exited the sensing channel are inaccurate due to perturbation of the measuring interface by the particle; at the time the particle exits the channel, the fluid is forced to move around the particle, which displaces the fluid interface used to measure the induced resistance.

2.2 Particle preparation

Gelatin Particles. Gelatin micro particles were selected because they are easy to manufacture, they exhibit uniform properties and have no internal structure. Gelatin particles were made using a solution 5% (w/v) of gelatin (Sigma Aldrich) emulsified in light mineral oil (Mallinckrodt Chemicals). Span 80 (Sigma-Aldrich) was added to the oil at 1% (v/v) to stabilize the droplets against coalescence. Gelatin solution was prepared by dissolving gelatin into water at 70 °C while agitating to achieve complete mixing. The gelatin solution was added to light mineral oil to form a biphasic solution of 1% (v/v). Then, the solution was vortexed at speed 6 using a VWR Analog Vortex Mixer, which created the particles to be analyzed by the comparator. The solution was stored at 4 °C for 3 h prior to use.

HL-60 Cells. HL-60 cells, a promyelocytic leukemia cell line, were cultured according to supplier protocol (ATCC). The cells were washed two times with a solution of PBS. Then, the media was replaced with the High Viscosity Media; a solution made of 9.1 mL PBS, 9 g dextran (MW = 2×10^6) (Sigma Aldrich), 0.1 g BSA, and 0.04 g Pluronic, F-108 (Sigma Aldrich). At the same time, PDMS devices were incubated with High Viscosity Media for 30-60 min at 20 °C (Room Temperature). HL-60 cells were selected as an alternative to gelatin particles to demonstrate that the response time delay is also presents in other systems, and it is a consequence of the fluid mechanics rather than the type of particle measured. HL-60 cells were selected because there are approximately spherical, hence they deform uniformly as they traverse the measurement channel, and their mechanical properties have been previously studied (Rosenbluth et al. 2006; Sirghi et al. 2008).

3. Results and discussion

3.1 Differential Manometer Analysis and Design

At low Reynolds numbers ($Re = \frac{uH}{\nu} \ll 1$, where u is the average velocity of the channel, H is the channel height, and ν is the kinematic viscosity of the fluid), the time taken by the particles to flow through the microchannel ($T \sim \frac{L}{u}$, where L is the sensing channel length) is much longer than the viscous dissipation time scale ($\tau = \frac{H^2}{\nu}$, the time it takes for fluid momentum to diffuse with

momentum diffusivity ν between the center of the channel and the channel wall); in other words if $Re \ll 1$ then $\frac{\tau}{T} \sim Re * \frac{H}{L} \ll 1$. As a result, fluid inertia effects can be ignored in the comparator's behavior at low Reynolds numbers. In the experiments reported in this paper, $Re \sim 0.01$ (unless noted otherwise), $T \sim 0.1$ s and $\tau \sim 0.04$ ms; then, the fluid inertia effects can be ignored. As a consequence, in the low Reynolds regime, the manometer can be modeled as a resistance network (**Fig. 2a & b**).

Using the resistance model, it is possible to determine the sensitivity of the differential manometer, i.e. the degree to which the interface displaced for a given hydrodynamic resistance induced by a particle in the sensing channel. In a shallow rectangular channel (a channel whose width is many times larger than its height), the fully-developed velocity profile in the central section of the channel width can be approximated as the velocity profile between parallel plates. In the flow between parallel plates, the velocity profile is independent of the position along the channel's width; hence the flow rate per unit width is approximately constant across the channel. The interface displacement Δy corresponds to a change in the ratio of the flows that come from the sensing and reference channels, and $2\Delta y/W$ can be approximated as the relative difference between the flows

coming from the reference and sensing channels: i.e. $\frac{I - I_{reference}}{I + I_{reference}}$ where I is the flow through the sensing channel and $I_{reference}$ is the flow through the reference channel. Then from the manometer equivalent circuit, the sensitivity can be calculated as

$$Sensitivity = \left| \frac{I - I_{reference}}{I + I_{reference}} \right| = \left| \frac{\frac{1}{R_{entrance} + R} - \frac{1}{R_{entrance} + R + \Delta R}}{\frac{1}{R_{entrance} + R} + \frac{1}{R_{entrance} + R + \Delta R}} \right|, \quad (1)$$

where R is the sensing resistance, ΔR is the induced change in resistance of the sensing channel and $R_{entrance}$ is the entrance resistance produced by the inlet channel and tubing. Notice that the bars for absolute value have been added to the sensitivity definition to make sensitivity positive valued. From the resistance analysis, it is clear that the sensitivity does not depend on the exit resistance, R_{exit} . Since the total flow rate in the circuit depends on the exit resistance that does not affect the manometer sensitivity, the exit resistance can be used as a free parameter to modulate the velocity range of the manometer without affecting the sensitivity of the device. The ability to modulate the velocity range is quite useful when only a limited pressure range can be imposed at the inlet. In this case the pressure range is limited by the experimental setup, the maximum pressure is set by device materials, ~ 20 PSI (maximum PDMS-glass plasma bonding strength) and the minimum pressure reliably provided by the pressure regulators, ~ 0.01 PSI.

If the induced resistance is small compared to the sensing resistance, $\frac{\Delta R}{R} \ll 1$, then linearization of Eqn. (1) allows the sensitivity to be expressed as

$$\left| \frac{I - I_{reference}}{I + I_{reference}} \right| = \left| \frac{\Delta R}{2(R_{entrance} + R)} \right|, \quad (2)$$

This linearized sensitivity can be used to estimate the interface displacement, Δy . Now, if the velocity profile along the flow direction (x direction), is considered constant across the channel width (y direction), a reasonable assumption for the central part of the measuring channel due to its large aspect ratio, width \gg height, then

$$\left| \frac{I - I_{reference}}{I + I_{reference}} \right| = \left| \frac{2\Delta y}{W} \right|, \quad (3)$$

where W is the measurement channel width. Now, combining the resistive (Eqn. 2) and geometrical (Eqn. 3) sensitivity estimations, we obtain the interface displacement as a function of induced resistance,

$$\left| \frac{\Delta y}{W} \right| = \left| \frac{\Delta R}{4(R_{entrance} + R)} \right| \quad (4)$$

Equations (1-4) suggest that $R_{entrance}$ must be minimized to maximize the sensitivity. Since the sensitivity does not depend on R_{exit} , it offers a way to tune the flow rate through the device without affecting the sensitivity.

After fabrication, in order to verify the accuracy of the fabricated devices, the relative resistances were extracted experimentally. The inlet channel resistance, $R_{entrance}+R$, and exit resistance, R_{exit} , can be determined experimentally by calibrating the device in the absence of any particles (**Fig. 3a**), as discussed later in the section “Interface displacement calibration”. Then, using the observed displacement of the interface, it is possible to calculate the pressure drop across the particle flowing through the sensing channel and the flow rates in the sensing channel. Additionally, optical imaging also enables simultaneous measurement of the velocity of the particles.

3.2. Differential Manometer Simulation

In order to design microfluidic differential manometers to measure hydrodynamic resistance, we performed numerical simulations of the interface displacement using commercially available multiphysics software, Comsol Multiphysics 7 (**Fig. 3**). Simulations were performed using full Navier-Stokes equations coupled to convective diffusion equations. In terms of boundary conditions, at all walls, except inlets and outlets, velocity was set to zero. At the upper sensing channel, a fluid with 0.001 Pa·s viscosity was injected at a constant velocity of 1.6 mm/s ($Re=0.01$, where Re is the Reynolds number). A flat-injection velocity profile was used instead of a more realistic parabolic-injection profile since the developing distance is extremely small, $\sim Re*H=0.06$ m. At the lower reference channel, a fluid with 0.001 Pa·s viscosity was injected to produce relative flow rates of 10:1, 5:1, 2.5:1, 1.25:1 and 1:1 ratios. Additionally the reference fluid was assumed to have a dilute dye with a diffusivity of 1×10^{-10} m²/s at a concentration of 0.1 mol/m³.

From the simulation it was observed that the steady state interface displacement depends heavily on the distance from the measuring junction, i.e. the junction formed by the measuring, reference and sensing channels (**Fig. 3b**). As the distance from the measuring junction increases, the interface displacement reaches a value independent of the measurement position downstream of the junction.

This position-independent displacement directly reflects the relative flow rates through the sensing and reference channels; on the other hand interface displacement measured close to the measuring junction depends additionally on the device geometry and position along the channel. Therefore, if the interface displacement is measured before the interface reaches the position-independent displacement, the displacement at each position should be characterized and related to the position-independent displacement.

3.3. Experimental characterization of the differential manometer

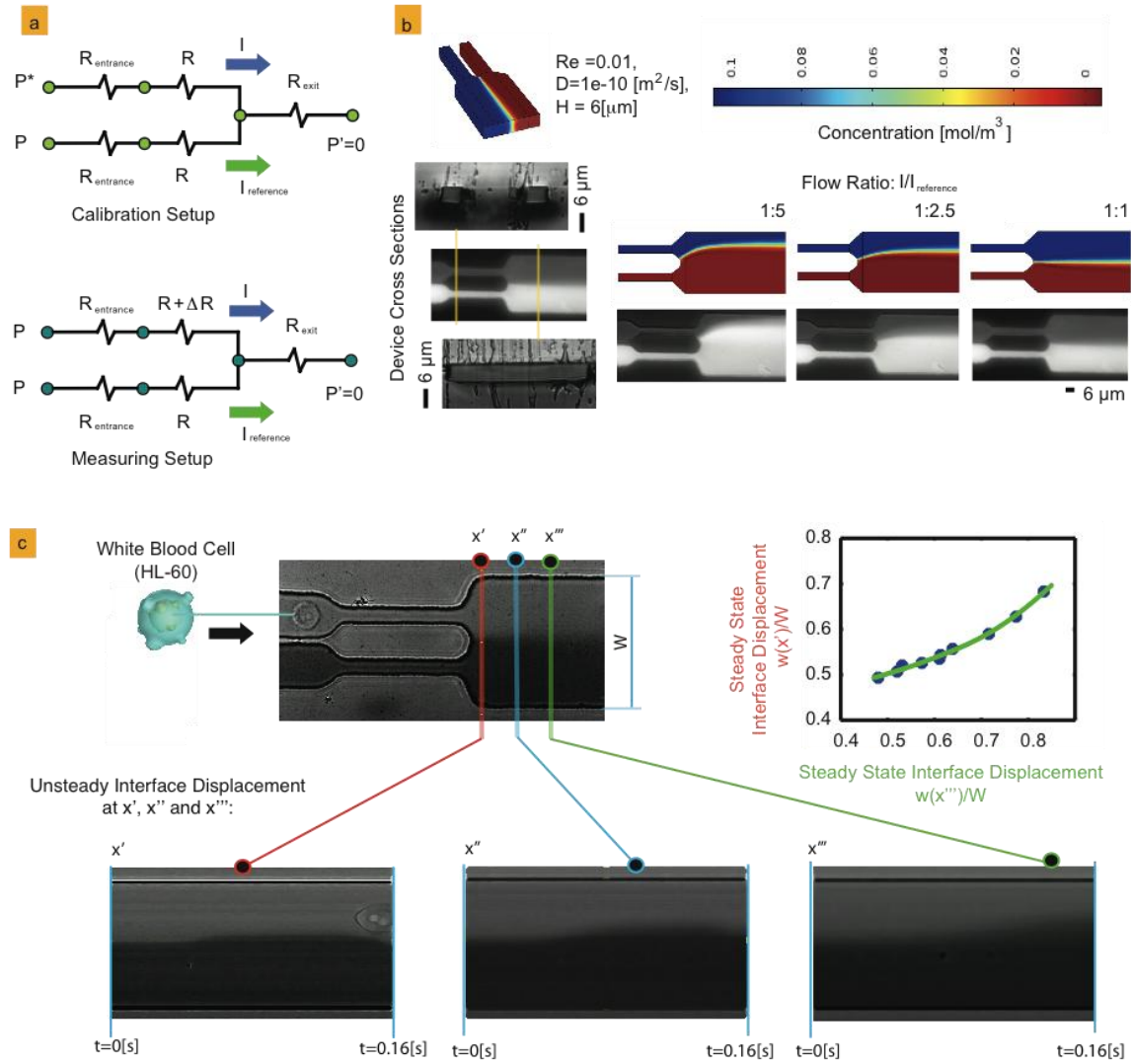


Figure 3. Interface displacements as a function of time and position along the measurement channel. a) Microfluidic circuit models used for calibration and measurement. b) Simulated and experimental interface displacements as a function of relative flow rates. c) Interface displacements at three positions (x' , x'' and x''') as a function of time as a particle (HL-60 cell) traverses the sensing channel. The panels represent displacement-time maps of the same video at x' , x'' , and x''' , showing that further away from the channel junction, the delay in response increases. A vertical line on the map corresponds to the pixels along the vertical line at x' (or x'' , x''') in the video at the time indicated on the horizontal axis. Inset: Steady state interface displacements at points x' and x''' .

Comparator sensitivity

To verify the accuracy of the simulations, devices were fabricated with similar geometries as the simulated ones, 6 μm square cross-section sensing channel of 50 μm length. Deionized water was flown through the sensing channel and water with FITC dextran (150 kDa) or Blue Dextran (150 kDa) was flown through the reference channel. The simulation interface displacement results agreed with the experimental results. As predicted by the simulation, the interface was blurred due to diffusion. Despite the fact that dextran has a diffusivity smaller than the simulated one, $0.2 \times 10^{-10} \text{ m}^2/\text{s}$, the experimental diffusivity blurring is similar to the simulated one. In the experiments, additional blurring might be caused by diffusion of the dye into the PDMS matrix, which causes a permanent level of background fluorescence (evident upon variation of the flow rates after prolonged exposure to the dye).

Convective delay and convective time scale

In order to measure the time it takes for the interface to react to the passage of particles through the sensing channels, two kinds of particles were used: gelatin particles and cells (HL-60 cells), as described in the Materials and Methods section. Despite the fact that the microfluidic devices were designed such that the unsteady time scale, $<0.001 \text{ s}$, is much smaller than the particle transit time through the sensing channel, $>0.1 \text{ s}$, the interface at the measuring channel does not respond as fast for both gelatin particles and cells; furthermore, the delay in response of the interface displacement grows as the distance from the measuring junction increases (**Fig. 3c**). Convective transport is responsible for the slower response. Even when the velocities at every single point inside the microfluidic channel change from one steady state to another after a couple of viscous dissipation

time constants ($\tau = \frac{H^2}{\nu}$), the dyed fluid takes additional time to replace the colorless fluid that was occupying the channel beforehand, thus creating a convective transport delay.

The convective transport scale can be estimated from basic control volume analysis (**Fig. 4**). Using the depicted control volume and analyzing just the reference fluid

$$\frac{\partial(H \int_0^{L_{cv}} y dx)}{\partial t} - I_{reference} + \int_0^h \int_0^H u_{out} dy dz = 0, \quad (5)$$

where H is the channel height, $y(x)$ is the interface position at a position x along the measuring channel, L_{cv} is the length of the control volume along the x direction and u_{out} is the fluid velocity at the exit of the control volume. The first term denotes the change in the volume of the reference fluid in the control volume, the second term denotes the inflow of the reference fluid from the left into the control volume, and the third term denotes the outflow of the reference fluid through its right side. Further, the expression can be simplified if the first integral is known, hence we write the integral in a simpler form as

$$\frac{\partial(H \int_0^{L_{cv}} y dx)}{\partial t} = HL_{cv} \alpha \frac{\partial h}{\partial t}, \quad (6)$$

Where h is the interface position, α is a constant that depends on the geometry and control volume length L_{cv} ($\alpha = 1$ for a horizontal displacement of the interface and $\alpha = 0.5$ for a displacement that grows linearly with the distance from the channel junction). Now, using the Laplace transform,

$$\alpha HL_{cv} \frac{\partial h}{\partial t} \rightarrow HL_{cv} \alpha (s * h - 0.5W). \quad (7)$$

Also, if we assume that the velocity field has reached steady state

$$\int_0^h \int_0^H u_{out} dy dz \approx u_{out} * Hh \approx I_{Rexit} * (h/W), \quad (8)$$

where u_{out} is the average velocity at the control volume exit and I_{Rexit} is the flow rate through the measuring channel. Finally, substituting the terms back together

$$HL_{cv} \alpha (s * h - 0.5W) - I_{reference} / s + I_{Rexit} * (h(s)/W) = 0, \quad (9)$$

or

$$\frac{h(s)}{W} = \frac{\frac{I_{reference}}{s} + 0.5W\alpha HL_{cv}}{I_{Rexit}} = \frac{I_{reference}}{(I + I_{reference})} \frac{0.5W\alpha HL_{cv} / I_{reference} s + 1}{s[(\alpha WHL_{cv} / I_{Rexit})s + 1]} =$$

$$\frac{I_{reference}}{I + I_{reference}} \left[\frac{1}{s} + \frac{0.5W\alpha HL_{cv}}{(\alpha WHL_{cv} / I_{Rexit})s + 1} \left[\frac{I - I_{reference}}{I + I_{reference}} \right] \right], \quad (10)$$

therefore, as a first approximation, the convective delay acts as a low pass filter with characteristic time constant $\sim \alpha WHL_{cv} / I_{Rexit}$. The convective time delay increases with control volume length, L_{cv} , device height, H , and width W . Further, the time delay is inversely proportional to the exit flow rate, which is highly convenient for our purposes since as the transit time decreases the delay decreases too. Therefore if the convective time delay is smaller than the transit time at a specific injection pressure, the time delay will remain small at a higher injection pressure. In this case, if

$W \sim 24 \mu m$, $H \sim 6 \mu m$, $L_{cv} \sim 2 \mu m$ and $I_{Rexit} \sim 1 \frac{mm}{s} * 36 \mu m^2$ then the characteristic time

constant is $\sim 4 ms$, smaller than the transit time $> 10 ms$. Since the convective time is small but not negligible, the measuring distance L_{cv} must be kept as small as possible and measuring should be done as close to the sensing junction as possible.

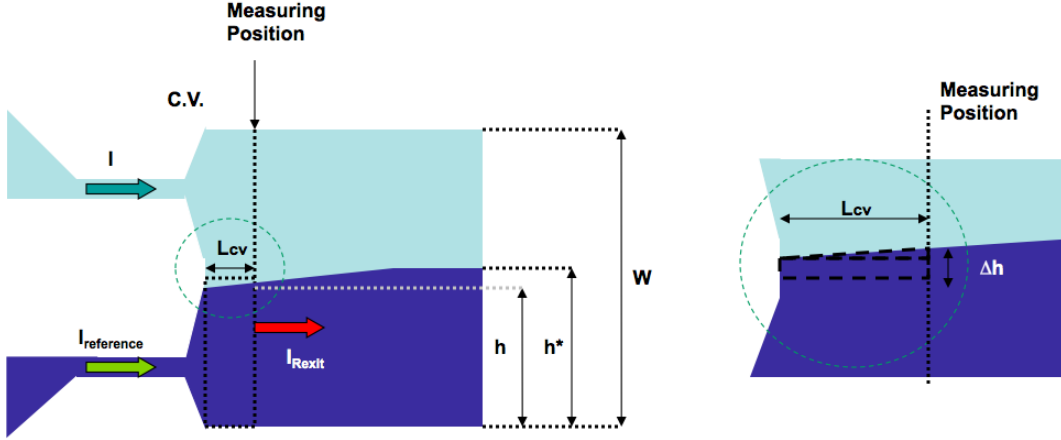


Figure 4. Schematic depicting the control volume used in the convective timescale analysis of the differential manometer.

Capacitive delay and capacitive timescale

When dealing with devices fabricated with compressible materials, e.g. polymeric microfluidic devices made of PDMS, an additional time scale should be considered: the compressive or capacitive timescale. As the average pressure through a microfluidic channel section changes, it deforms to accommodate the new pressure forces. The pressure-induced deformation increases or decreases the channel volume, which creates capacitive transients even though the fluid is incompressible. The effects of the volume change can be estimated if capacitive elements are added to our resistive model.

Using the Lamé's solution for the plain strain case (Gao 2003), and linearizing the equations for small deformations for a cylindrical channel within an infinite solid deformable domain,

$$\Delta Vol = (P' - P_{exit}) \frac{2\pi a^2 \lambda (1 + \nu)}{E}, \quad (11)$$

where P' is the average channel pressure, P_{exit} is the atmospheric pressure outside the microfluidic channel, a is the channel radius, λ is the channel length, ν is the Poisson ratio, E is the channel wall Young modulus ($E \sim 400$ kPa), and ΔVol is the volumetric change due to the channel compressibility. Therefore the capacitance of the channel (C), is

$$C = \frac{2\pi a^2 \lambda (1 + \nu)}{E}. \quad (12)$$

If we consider a rectangular channel, then under small deformations,

$$\Delta Vol \approx (P' - P_{exit}) \frac{\beta WH \lambda (1 + \nu)}{E}, \quad (13)$$

and

$$C \approx \frac{\beta WH \lambda (1 + \nu)}{E}, \quad (14)$$

where β is a number of order 1 that depends on the ratio W/H , where W is the channel width and H is the channel height. Now, assuming $\beta=1$, we can approximately incorporate the capacitive effects into the resistive model. When incorporating the capacitive effects generated by channel compression, we have two options. The first approach is to add the capacitive elements between the middle section of the channel resistance and the outlet pressure; which accurately imposes the average pressure into the capacitive element but since each resistance is split in two this approach generates additional resistive elements and nodes in the lumped model. The second approach is to connect the capacitive elements at the ends of resistances, which minimizes the number of elements and nodes in the model but could fail to capture the capacitive effects properly in simple systems, e.g. a single channel connected to a variable pressure. The equivalent circuits for both approaches are depicted in **Fig. 5**, where the inlet resistance has been divided into tubing resistance, R_{tubing} , and entrance channel resistance, R_{entrance} , to adequately incorporate the channel capacitances. The Simulink model is depicted in Appendix 1.

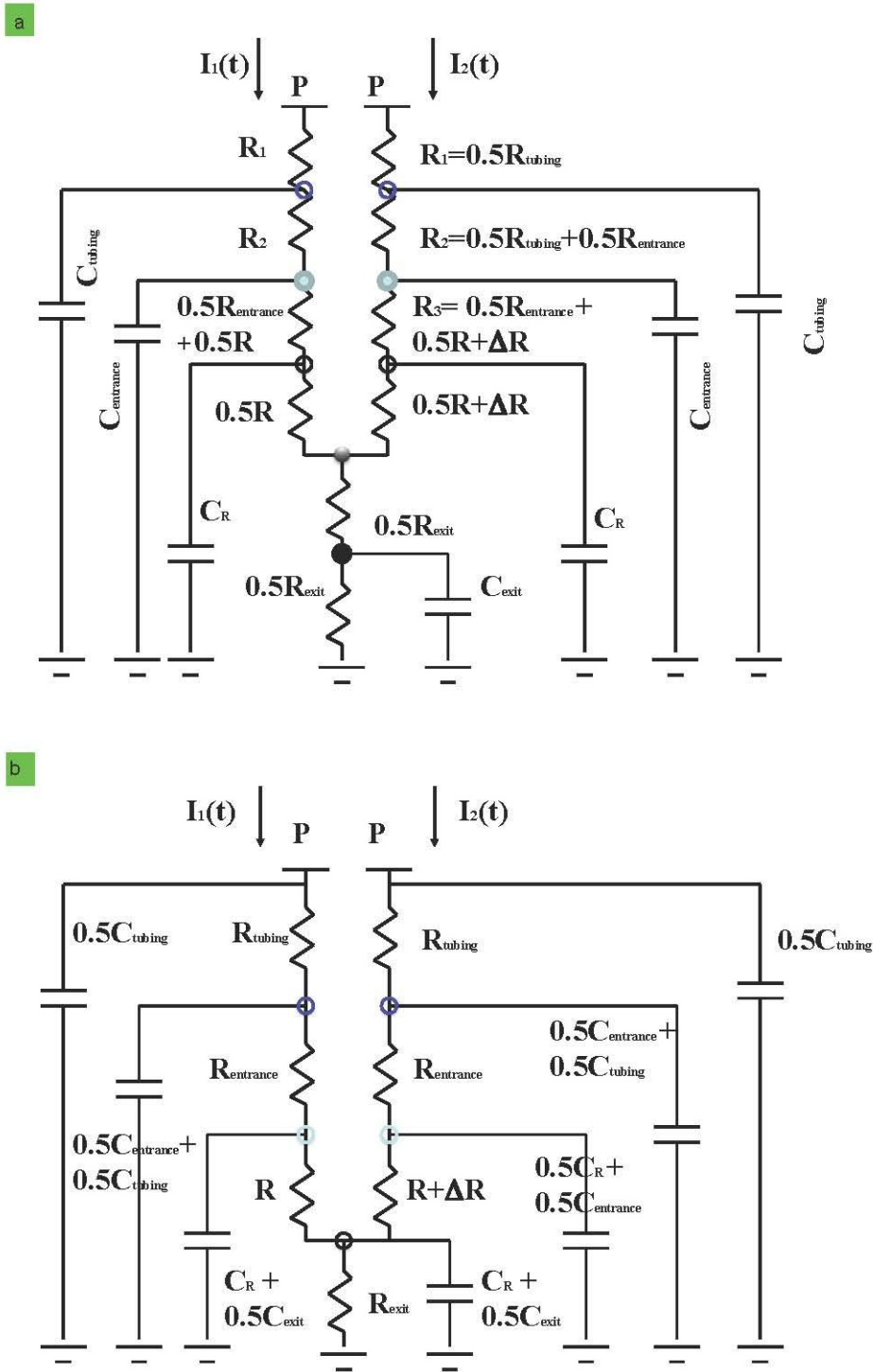


Figure 5. Manometer equivalent circuit with capacitive effects incorporated. a) Capacitive effects incorporated at each of the channels midsection. b) Capacitive effects incorporated at the channels inlet and outlet sections.

Since the resistance measurement relies only on the relative flow rates between the reference and sensing channels, the capacitive delay can be estimated by calculating the different RC constants of the injection channels of the device in **Fig. 5a**. First, notice that the resistive and capacitive network is similar to the capacitive coupling networks used in high frequency circuits. Hence, with this similitude in mind, we can visualize the capacitances as impedances whose absolute magnitude is a function of frequency, and hence time, that couple the comparator's junction to the power supply, i.e. pressure supply. As a first order analysis and to gain intuitive understanding of the circuit we can calculate the effective time scale of each coupling capacitor in our circuit. Capacitors whose response time is much shorter or much larger than the cell passage time can be neglected in estimating the response time of the microfluidic comparator.

For the 6 μm channel width manometer, the capacitance of the sensing channel is $\sim C_R = 5.6 \times 10^{-21} \text{ m}^3 \cdot \text{Pa}^{-1}$ and the resistance of the associated reference channel is $R = 1.5 \times 10^{15} \text{ Pa} \cdot \text{s} \cdot \text{m}^{-3}$; therefore the time constant for this section of the device is $\sim 0.5 \cdot R \cdot C_R = 0.004 \text{ ms}$, which is much smaller than the cell passage time, $> 10 \text{ ms}$. The capacitance of the tubing, C_{tubing} , is $2 \times 10^{-14} \text{ m}^3 \cdot \text{Pa}^{-1}$. In this case, the associated resistance is $\sim R$ which corresponds to a response time of $\sim R \cdot C_R = 3 \text{ s}$, which is much larger than the cell passage time. Finally, the capacitance at the entrance channel is $\sim C_R = 1.6 \times 10^{-18} \text{ m}^3 \cdot \text{Pa}^{-1}$; therefore the time constant associated with the entrance channel capacitor is $\sim R \cdot C_{\text{entrance}} = 2.4 \text{ ms}$, which is smaller than the cell passage time, but of the same order of magnitude. Then the capacitance of the sensing channel and tubing operate at completely different time scales when compared to the cell transit time. Hence, the time delay is dominated by the entrance channel capacitance.

Simulink simulation of delay effects

Using the resistance models with added capacitance it is possible to simulate any delay in the resistance measurement. Simulink was used to numerically implement the resistive-capacitive model (**Fig. 5**). In order to simulate a sudden resistance change a step function of magnitude $0.1R$ and 10 ms duration was implemented as system input. From the simulation incorporating capacitances at the channel inlet and outlets, it was observed that the comparator's resistance readout had an initial fast rise, $< 1 \text{ ms}$, to $\sim 60\%$ of the final steady value followed by a slower rise to final value of $\sim 3 \text{ ms}$, after which the resistance readout reached a steady state (**Fig. 6**). Similarly, from the simulation incorporating capacitances at the middle of the channels, it was observed that capacitive effects produce a delay of roughly 2-3 ms, after which the resistance readout reaches a steady state. From both simulations it is clear that the manometer is only adequate to measure cells with transit times larger than 3 ms.

Further, using Eqn. 10 we can incorporate the convective effects as a low pass filter. (Eqn. 10 relates the change in flow rates to the change in the interface position in the Laplace domain and has the mathematical form of a low pass filter). When adding the convective effects of measuring 2 μm away from the junction, the delay grows to reach 7-9 ms, which is just sufficient to allow for resistance measurement (**Fig. 7**). In this case, the delay is an upper limit estimate since the channel capacitance was overestimated by assuming bottom and upper channel walls to be equally elastic. Further, since the velocity at the interface was assumed to be equal to the average velocity, the convective delay is also an upper limit. In reality half of the channel is made out of glass, practically incompressible for the pressure range used, which sets the value of β . Additionally, from the simulation is clear that although capacitance produces a non-negligible effect in the delay, the dominant physical effect creating a delay in the manometer readout is the convective transport.

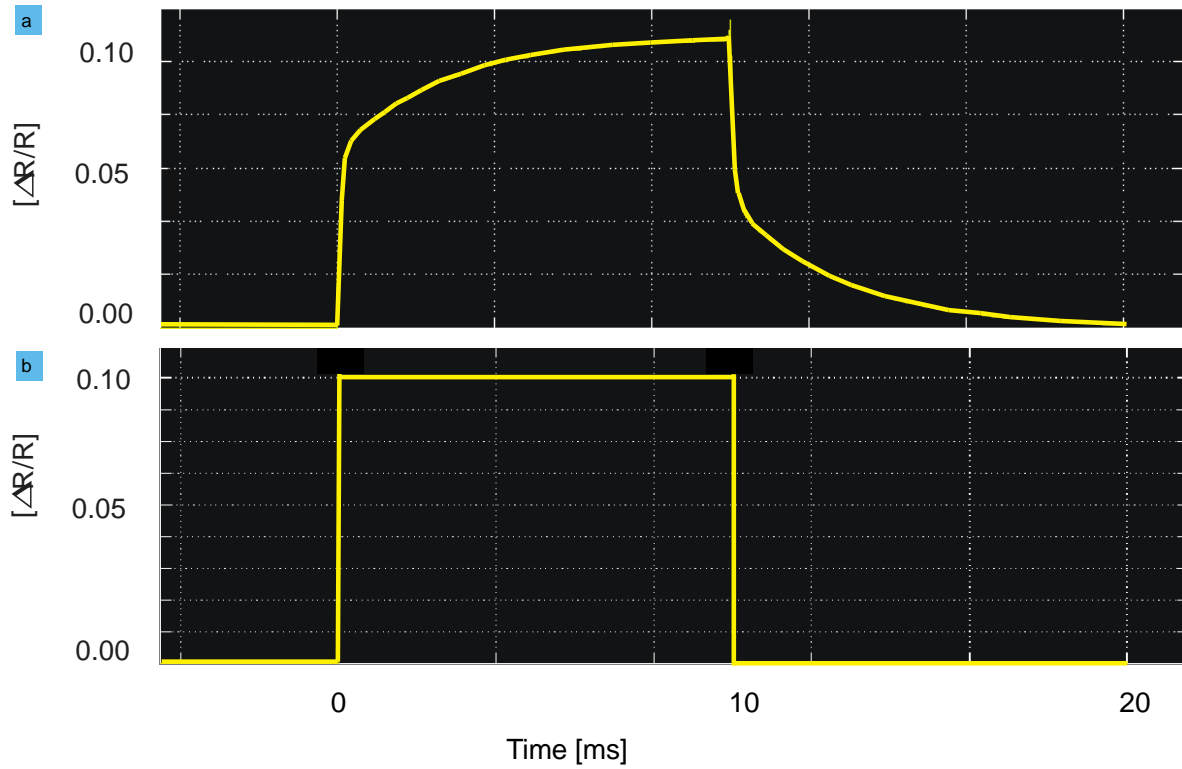


Figure 6. Simulink results of manometer readout with capacitive effects incorporated. Capacitances were added at the channel middle section. a) Simulated resistance readout once capacitive effects are incorporated. b) Step input function that simulates the induced resistance.

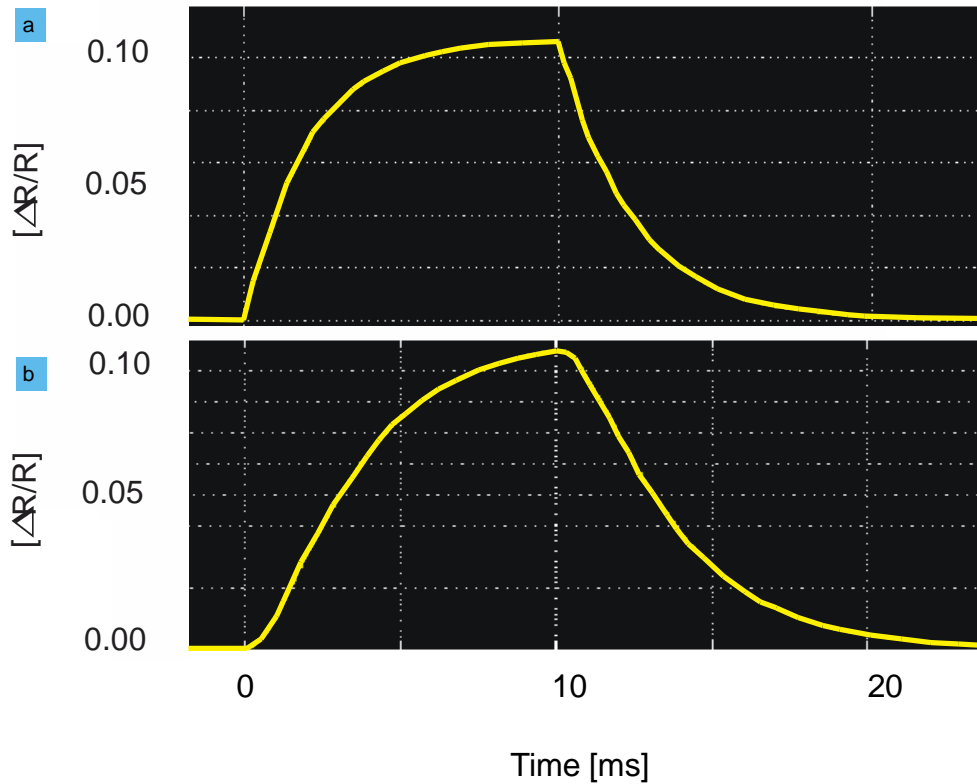


Figure 7. Simulink results of manometer readout with capacitive and convective effects incorporated. Capacitances were added at the channel input and output. a) Simulated resistance readout once capacitive effects are incorporated. b) Simulated resistance readout with capacitive and convective effects included.

Interface displacement calibration

As discussed in the previous section, in order to avoid convective delays, the steady state interface displacement must be measured as close as possible to the measuring junction. Nevertheless measuring the interface close to the junction has its own difficulties. The interface displacement close to the junction depends on the distance from the junction as well as the relative flow rates. Hence calibration must be performed to relate the position-independent displacement to the displacement at the measuring position. Calibration can be done numerically or experimentally (**Fig. 8**). Here the experimental calibration is discussed.

A single calibration and measurement of the interface displacement as a function relative flow rates is necessary and sufficient at low Reynolds numbers provided that diffusion effects are negligible, i.e. the calibration is independent of the Re number (see Appendix 1).

Interface calibration can be done by measuring the interface displacement at different flow rates or by modulating the injection pressures. Setting different flow rates can be implemented by injecting

fluids with a syringe pump in a relatively easy fashion. Nevertheless, due to the compressibility of the tubing, syringes and device materials, the steady state can take from minutes to hours to be achieved; which makes calibration cumbersome. An alternative is to apply different injection pressures at the device inlets.

Additionally, if injection pressures are modulated to calibrate the manometer circuit, the pressures can also be used to extract relative values of the circuit resistances. If the pressure changes at one of the inlets by a small amount, i.e. $P^* = P + \Delta P$ where $\Delta P \ll P$, then the relative change in flow rates can be calculated using the resistive circuit model (**Fig. 3**). Then

$$\frac{I - I_{reference}}{I + I_{reference}} = \frac{\Delta P / P}{2 \left(1 - \frac{2R_{exit}}{2R_{exit} + R_{entrance} + R} \right)}, \quad (15)$$

from which calibration can be achieved since we know that

$$\frac{I - I_{reference}}{I + I_{reference}} = \frac{2\Delta y}{W}, \quad (16)$$

hence

$$\frac{\Delta y}{W} = \frac{\Delta P / P}{4 \left(1 - \frac{2R_{exit}}{2R_{exit} + R_{entrance} + R} \right)}. \quad (17)$$

Therefore, if we obtain experimentally the relationship between the pressure and displacements for small pressure variations, i. e. the linearized pressure-displacement calibration, this relationship can be used to infer the value of $\frac{2R_{exit}}{2R_{exit} + (R_{entrance} + R)}$ by substituting it in (17). Then if we know

$\frac{2R_{exit}}{2R_{exit} + (R_{entrance} + R)}$, we can obtain the relative value of R_{exit} and $(R_{entrance} + R)$ and compare it with the value from the resistive model used during device design. For the differential manometers designed and fabricated, the relative value of R_{exit} and $(R_{entrance} + R)$ was within 5% of the design values, indicating a reasonable fabrication process.

An example of the calibration performed for every variation of the manometer geometry is shown in **Fig. 8**, where the fractional or relative displacement at the measuring position is plotted as a function of the position-independent displacement for a microfluidic manometer of 16 μm square channels, a larger cross section that allowed for a wider velocity range. From the calibration plot, it can be observed that minimizing the signal lag by measuring the interface displacement close to the measuring junction comes at a price; the sensitivity of the displacement at the measuring junction is smaller than the position-independent sensitivity measured downstream, in this case by a factor of roughly two. The calibration function is not linear, but can be linearized for small flow-ratio intervals at low Reynolds numbers, when the calibration function is a strictly growing positive function. At moderate and high Reynolds numbers, $Re > 1$, the calibration curve function first grows

and then decreases as a function of the position-independent displacement. As a consequence, calibration of the full calibration curve must be performed.

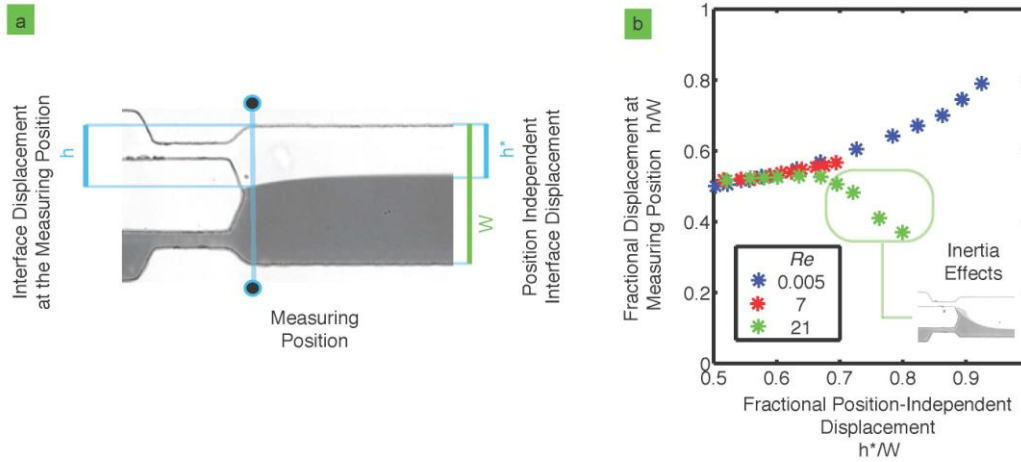


Figure 8. Interface displacements calibration as a function of Reynolds numbers. a) Micrograph showing the position where the interface displacements were measured. b) Fractional interface displacement as a function of relative injection pressures.

Further, when the velocity through the devices is such that $Re \sim 1$ or larger, the usage of the concept of hydrodynamic resistance should be avoided since the flow rate is not directly proportional to the pressure gradients, preventing the use of the Stokes equation. Even when the manometer can still be used to measure flow rates at moderate Re numbers, relating the velocity within the channels to the pressure drop and forces within the channel becomes challenging. At moderate Re numbers, before turbulence onset, a reasonable approximation is the use of the unsteady Bernoulli equation instead of the Stokes equation. Additionally, measuring the interface close to the measuring junction becomes challenging since the interface suffers the effects of the flow inertia. In order to explore the effects of flow inertia, the interface displacement close to the measuring junction was characterized for $Re = 0.005, 7$ and 21 (Fig. 9). As the Re number increases, the interface close to the measuring junction becomes less sensitive to the flow rate changes due to pressure or resistance variations. Further, at $Re=21$, the function that related pressure variations to interface displacement changes from being a strictly monotonic function to a function that first grows at small pressure ratios and decreases at higher pressure ratios. Finally, at $Re=21$ and when the flow ratios are larger than 2:1, the interface between dyed and non-dyed liquids becomes completely three-dimensional, and cannot be completely described by a 2D image (the surface cannot be generated by a single line that translates uniquely in the z direction). As a result of the new 3D geometry, the interface in the videos has two jumps instead of one. The change of the interface to a completely 3D surface is caused by the non-uniformity of the velocity profile along the measuring channel width.

The flow at the outlet of the channel with higher flow rate can be considered as a flow expansion, i.e. a jet expansion. In a flow expansion, a high-velocity fluid coming from a tube or pipe is incorporated into an infinite reservoir with stagnant fluid at the outlet of the tube. As the high-velocity fluid moves further away from the tube outlet, it slows down by redistributing its momentum to the stagnant fluid, entraining the previously stagnant fluid. Eventually, far away from the tube outlet, the fluid from the jet and the fluid surrounding it attain similar velocities and fluid-velocity goes down. In a jet, as the fluid-velocity at the pipe outlet increases, the distance to attain

uniform velocity increases. If we were to color the fluid coming from a jet expansion, we would observe a thin cylinder of liquid whose radius expands as it moves away from the tube outlet and which eventually mixes with the surrounding liquid.

Similar to what happens in a jet expansion, the fluid in a microfluidic comparator is also affected by inertia; but unlike a jet expansion, the presence of the walls imposes zero velocity boundary conditions at the closest and furthest x-y planes. Due to the presence of the walls, the fluid behaves differently at different x-y planes, depending on their distance from the shallow walls, closest and furthest x-y planes. Close to the walls, the effects of viscosity are large enough such that the interface behaves similarly to the low Re case. At the center of the channel, mid x-y planes further from the walls, the exit velocity is larger and as a consequence it takes a longer distance to achieve momentum redistribution and a uniform velocity profile, i.e. the distance to attain position independent interface displacement grows as Re grows.

The measuring interface is composed of streamlines at the center of the channel and streamlines close to the channel's upper and lower walls. The streamlines at the center will expand slowly (due to their higher inertia) while the streamlines at the walls will expand faster (due to the decreased inertia), causing the double interface jump in the image (Fig. 8 inset and Fig. 9b, bottom right panel). The extent of the velocity non-uniformity can be inferred from the developing length magnitude obtained from Blasius boundary layer solution, i.e.

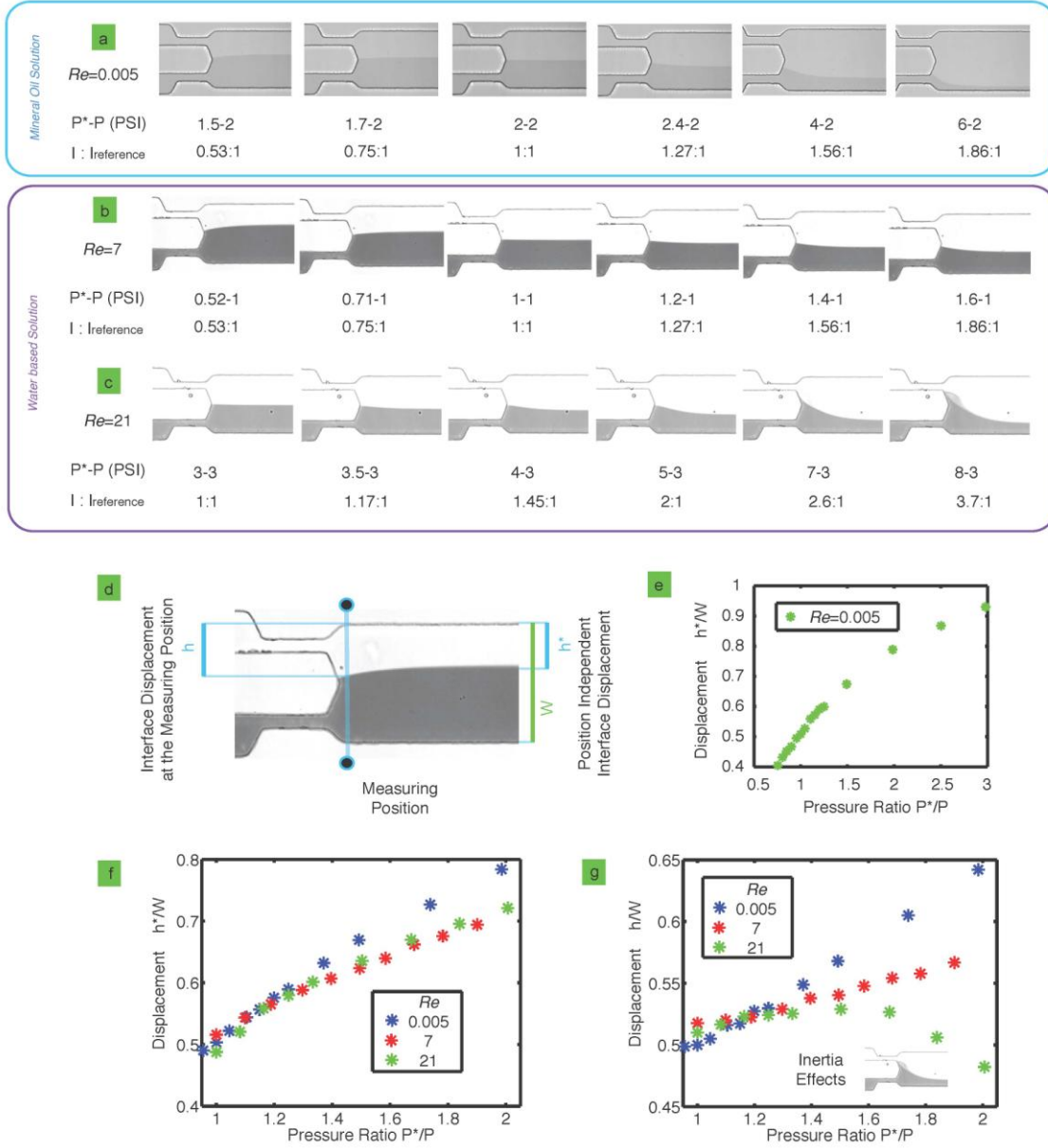


Figure 9. Interface displacements at the measuring position as a function of Reynolds number. a) Interface displacements at $Re=0.005$. Oil was used to reduce flow rates without reducing the injection pressure, preserving the accuracy of the applied pressure that was limited by the experimental setup. b & c) Interface displacements at $Re=7$ & 21 respectively. Water solutions were used to calibrate the manometer interface displacement. d) Micrograph showing the position where the interface displacements were measured. e) Position independent interface displacement as a function of relative injection pressures for low Reynolds numbers, $Re=0.005$ at the reference flow injection channel. f) Position-independent interface displacement as a function of relative injection pressures and Reynolds numbers at the reference channel. g) Interface displacements at the measuring position as a function of relative injection pressures and Reynolds numbers at the reference channel. Notice the interface double jump at the inset of Fig. 9 due to inertial effects.

$$\delta(l) \sim \frac{5l}{\sqrt{Re_l}} \sim \frac{H}{2}, \quad (18)$$

or

$$l \sim Re_H * \frac{H}{10}, \quad (19)$$

where δ is the boundary layer thickness, l is the developing length, Re_l is the Reynolds number as a function of the developing length and H is the channel height. From this approximation is obvious that the developing length depends linearly on the Re number, hence when $Re \ll 1$, the developing length can be neglected, but when $Re > 1$, it must be considered in all cases since $l \sim O H$.

5. Conclusions

In this paper we have analysed and characterized a microfluidic manometer. We determined that the manometer sensitivity is affected only by the resistances upstream of the measuring junction, and in order to maximize the sensitivity, the entrance resistances should be minimized. We have studied the physical factors that can cause a delay in the measured induced resistance: channel capacitance due to channel deformation and convective delay. We determined that the leading factor causing a delay in the resistance readout is the convective delay. Further, we determined that in order to avoid any signal delay, the interface displacements should be measured as close to the measuring junction as possible. Using numerical simulations and experiments, we determined that close to the measuring junction, the interface displacement is a function of the distance from measuring junction as well as the flow rates; in contrast, the interface displacement far away from the measuring junction is position-independent. Since interface displacement measurement close to the junction is desired, a calibration function relating the position-independent interface displacement to the interface displacement at the measuring position must be obtained. It was determined that at low Re numbers, aside from the convective effects, the calibration function is strictly monotonous and independent of Re ; while at moderate Re , a calibration must be performed for each velocity range since inertia effects affect the interface displacement close to the junction. Further, at moderate Re , the device sensitivity decreases and the calibration function is not necessarily positive-defined.

Microfluidic manometers offer a new opportunity to probe the biomechanical properties of cells and organic matter. We expect that the present work will enhance the understanding of microfluidic manometers, helping to enable a promising technology for the measurement of micro-particles and biological samples. Currently there are challenges that still remain to be addressed; in particular sample throughput and system cost at high speeds. In order to measure a significant cell/particle population, a large number of images/samples must be processed each second, which requires an expensive high speed camera. As an alternative, the interface movement can be tracked with purpose specific optics, e.g. a laser light beam that is partially blocked by the colored liquid, which can potentially decrease costs. Flow cytometry, the standard tool for analysis of cell populations, can process >100,000 cells per second. At current velocities, a single comparator can process only 10-100 cells per second; hence device parallelization is required for high cell throughput. In principle such parallelization is possible due to the simplicity and small footprint (device area) used by each device. An array of 1000 comparators, which can fit in a 4" wafer, can provide a throughput in the range of a flow cytometer. Nevertheless, the microfluidic manometer is useful as a tool to

understand the dynamics and probe the flow of soft particles and droplets through narrow channels and conduits.

Acknowledgements We acknowledge financial support from the Mexican National Science Foundation, CONACYT grant 205899. Devices were fabricated in the Microsystems Technology Laboratory (MTL) at MIT. We thank Evelyn Wang, for the use of the high-speed camera, and Roger D. Kamm, Jongyoon Han and Todd Thorsen for helpful discussions.

6. Nomenclature

a	Circular channel radius
C_R	Sensing channel capacitance
$C_{entrance}$	Entrance channel capacitance
C_{exit}	Exit channel capacitance
C_{tubing}	Capacitance generated by the tubing connecting the device to the injection reservoirs
D	Particle diameter measured directly from micrographs
D_H	Square channel hydraulic diameter, equivalent to H
E	Young modulus
h	Interface position at different point of the control volume
H	Device height, in the square channel it is also its width and hydraulic diameter
HR	Hydrodynamic resistance
I	Sensing channel volumetric flow rate
$I_{reference}$	Reference channel volumetric flow rate
I_{Rexit}	Exit channel volumetric flow rate
L	Sensing channel length
p	Pressure scalar field
P'	Injection pressure at the channel inlet
P	Injection pressure
P^*	Injection pressure varied during calibration procedure
P_{exit}	Outlet pressure at the device outlet
Q	Sample channel mass flow rate
$Q_{reference}$	Reference channel mass flow rate
Re	Reynolds number
R	Sensing channel resistance
$R_{entrance}$	Entrance channel resistance
R_{exit}	Exit channel resistance
R_{tubing}	Resistance generated by the tubing connecting the device to the injection reservoirs
t	Time
u	Average channel velocity
\vec{u}	Velocity vector field
u_{out}	Velocity leaving the control volume through the measuring channel
u_{out}	Average velocity leaving the control volume through the measuring channel
w	Interface position at the measuring point

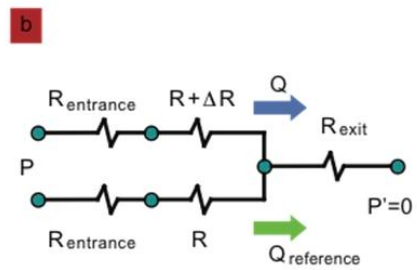
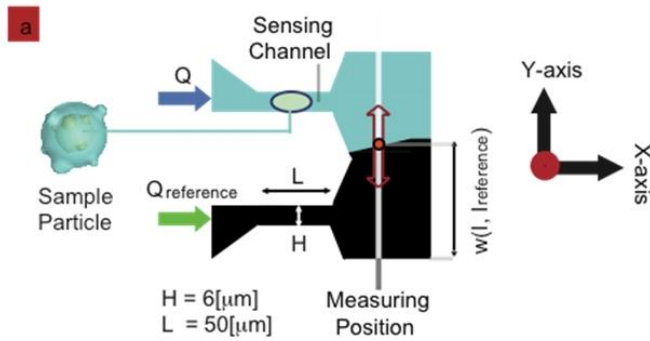
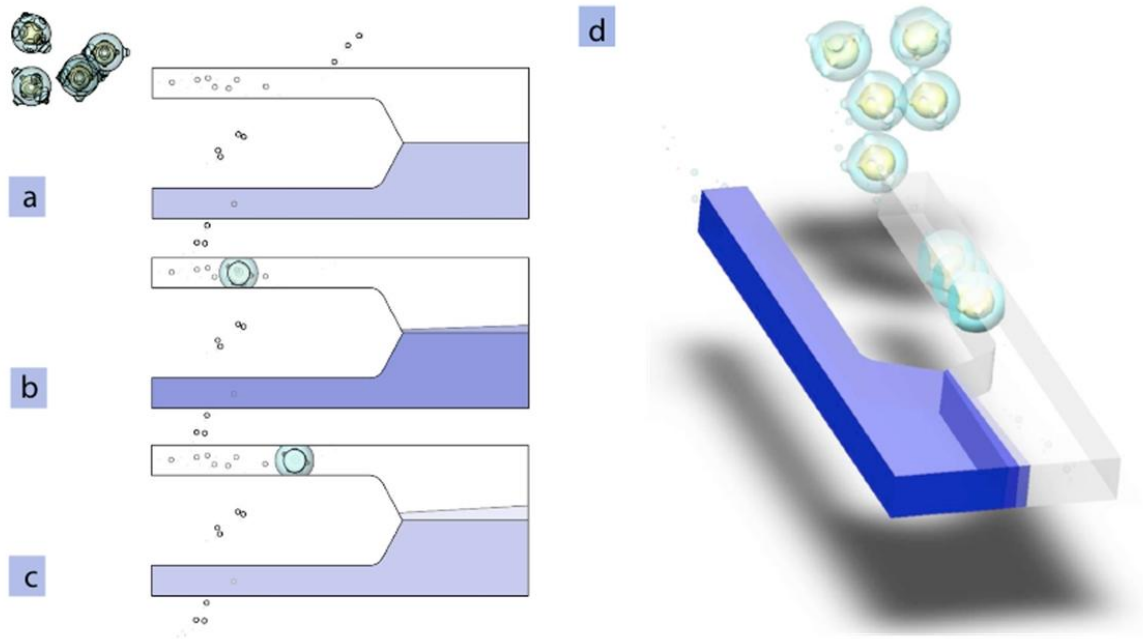
W	Measuring channel width
x	Horizontal coordinate
y	Vertical coordinate
z	Coordinate perpendicular to the paper plane
α^*	Proportionality constant
α	Proportionality constant that depends on the junction geometry
β	Positive and real constant
ΔR	Induced Hydrodynamic Resistance
ΔP	Small changes in injection pressure during manometer calibration
Δy	Induced interface displacement
λ	Channel length used in the capacitance calculations
μ	Dynamic viscosity of the media
τ	Inertial unsteady time scale
ν	Kinematic viscosity
ν	Poisson ratio

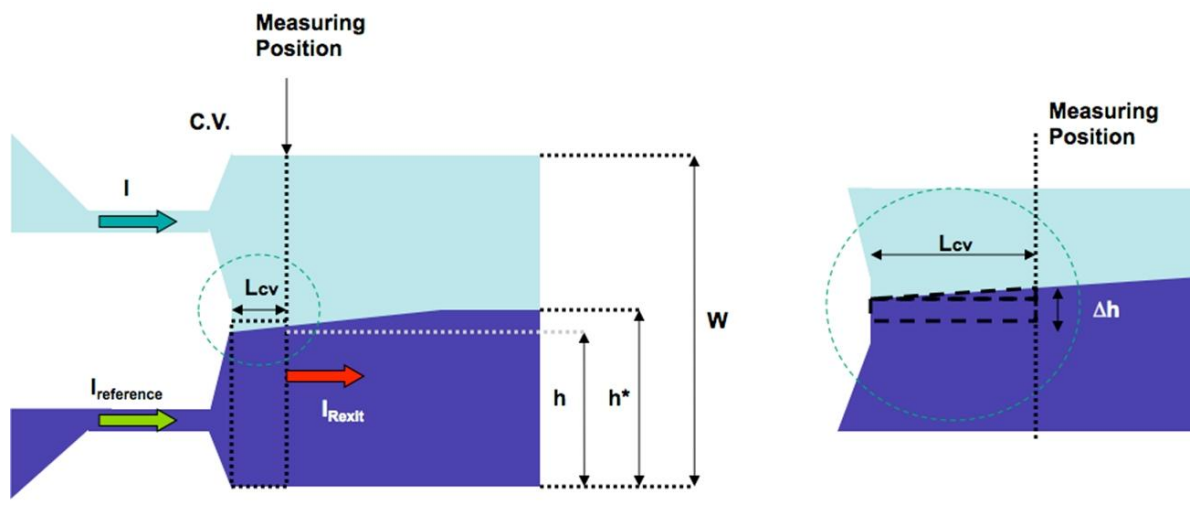
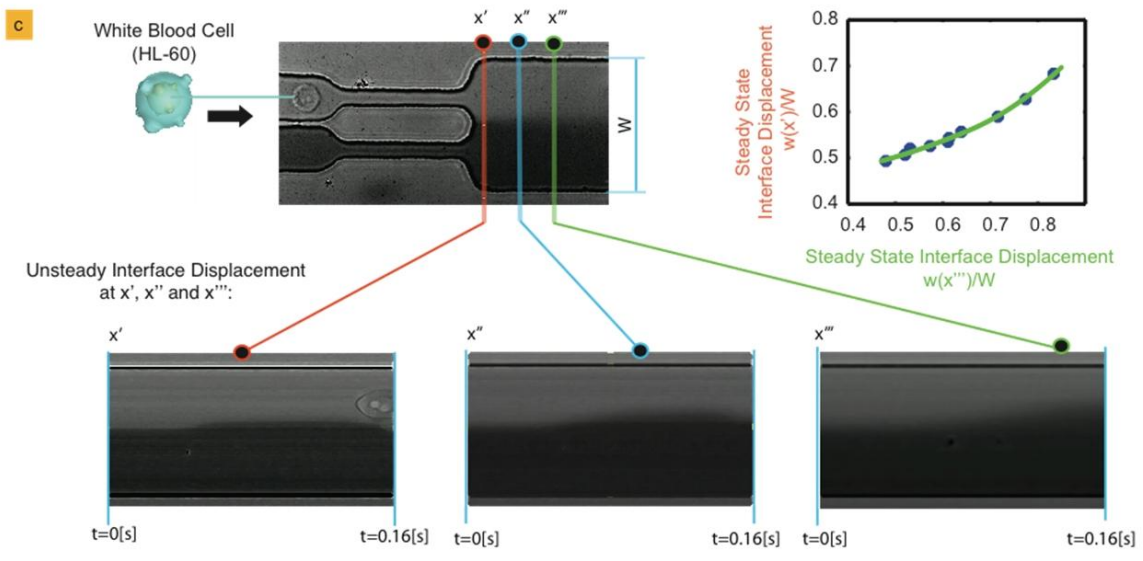
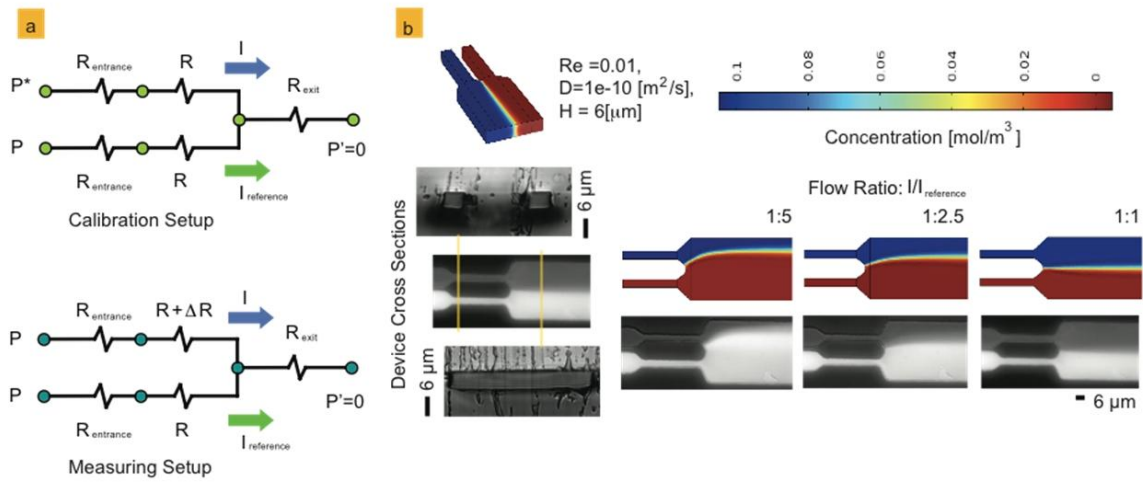
7. References

- Abkarian M, Faivre M, Stone HA (2006) High-speed microfluidic differential manometer for cellular-scale hydrodynamics. *PNAS* 103:538–542. doi: 10.1073/pnas.0507171102
- Abkarian M, Faivre M, Stone HA (2006) High-speed microfluidic differential manometer for cellular-scale hydrodynamics. *PNAS* 103:538–542. doi: 10.1073/pnas.0507171102
- Gao X-L (2003) Elasto-plastic analysis of an internally pressurized thick-walled cylinder using a strain gradient plasticity theory. *International Journal of Solids and Structures* 40:6445–6455. doi: 10.1016/S0020-7683(03)00424-4
- He M, Edgar JS, Jeffries GDM, et al. (2005) Selective Encapsulation of Single Cells and Subcellular Organelles into Picoliter- and Femtoliter-Volume Droplets. *Anal Chem* 77:1539–1544. doi: 10.1021/ac0480850
- Labrot V, Schindler M, Guillot P, et al. (2009) Extracting the hydrodynamic resistance of droplets from their behavior in microchannel networks. *Biomicrofluidics*. doi: 10.1063/1.3109686
- Mann S, Ozin GA (1996) Synthesis of inorganic materials with complex form. *Nature* 382:313–318.
- Pipper J, Inoue M, Ng LF-P, et al. (2007) Catching bird flu in a droplet. *Nature Medicine* 13:1259–1263. doi: 10.1038/nm1634
- Rosenbluth MJ, Lam WA, Fletcher DA (2006) Force Microscopy of Nonadherent Cells: A Comparison of Leukemia Cell Deformability. *Biophysical Journal* 90:2994–3003. doi: 10.1529/biophysj.105.067496

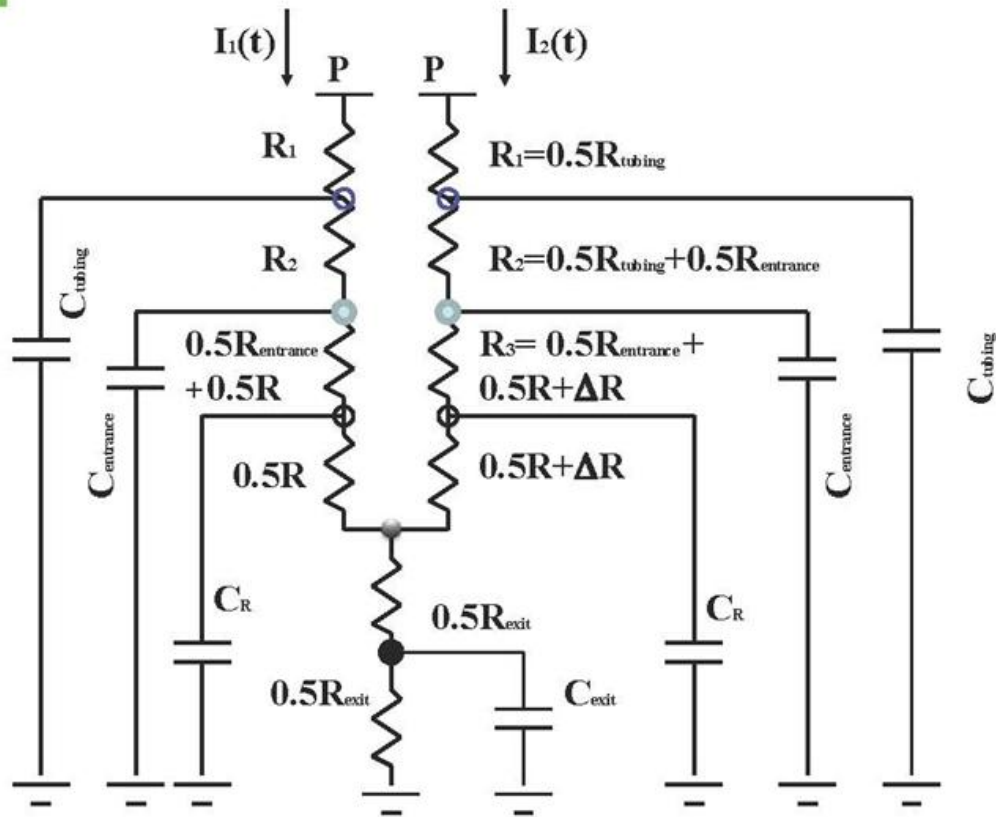
- Sessoms DA, Belloul M, Engl W, et al. (2009) Droplet motion in microfluidic networks: Hydrodynamic interactions and pressure-drop measurements. *Phys Rev E* 80:016317. doi: 10.1103/PhysRevE.80.016317
- Sirghi L, Ponti J, Broggi F, Rossi F (2008) Probing elasticity and adhesion of live cells by atomic force microscopy indentation. *European Biophysics Journal* 37:935–945. doi: 10.1007/s00249-008-0311-2
- Thorsen T, Roberts RW, Arnold FH, Quake SR (2001) Dynamic Pattern Formation in a Vesicle-Generating Microfluidic Device. *Phys Rev Lett* 86:4163–4166. doi: 10.1103/PhysRevLett.86.4163
- Vanapalli SA, Banpurkar AG, Van den Ende D, et al. (2009) Hydrodynamic resistance of single confined moving drops in rectangular microchannels. *Lab on a Chip* 9:982. doi: 10.1039/b815002h
- Vanapalli SA, Van den Ende D, Duits MHG, Mugele F (2007) Scaling of interface displacement in a microfluidic comparator. *Applied Physics Letters* 90:114109–114109–3. doi: 10.1063/1.2713800
- Vestad T, Marr DWM, Munakata T (2004) Flow resistance for microfluidic logic operations. *Applied Physics Letters* 84:5074–5075. doi: 10.1063/1.1764592
- Xu Q, Hashimoto M, Dang TT, et al. (2009) Preparation of Monodisperse Biodegradable Polymer Microparticles Using a Microfluidic Flow-Focusing Device for Controlled Drug Delivery. *Small* 5:1575–1581. doi: 10.1002/smll.200801855

Additional Figure 1. Simulink model of the manometer equivalent circuit with capacitive and convective effects incorporated. Capacitances are incorporated at the channel inlet and outlet in this example.

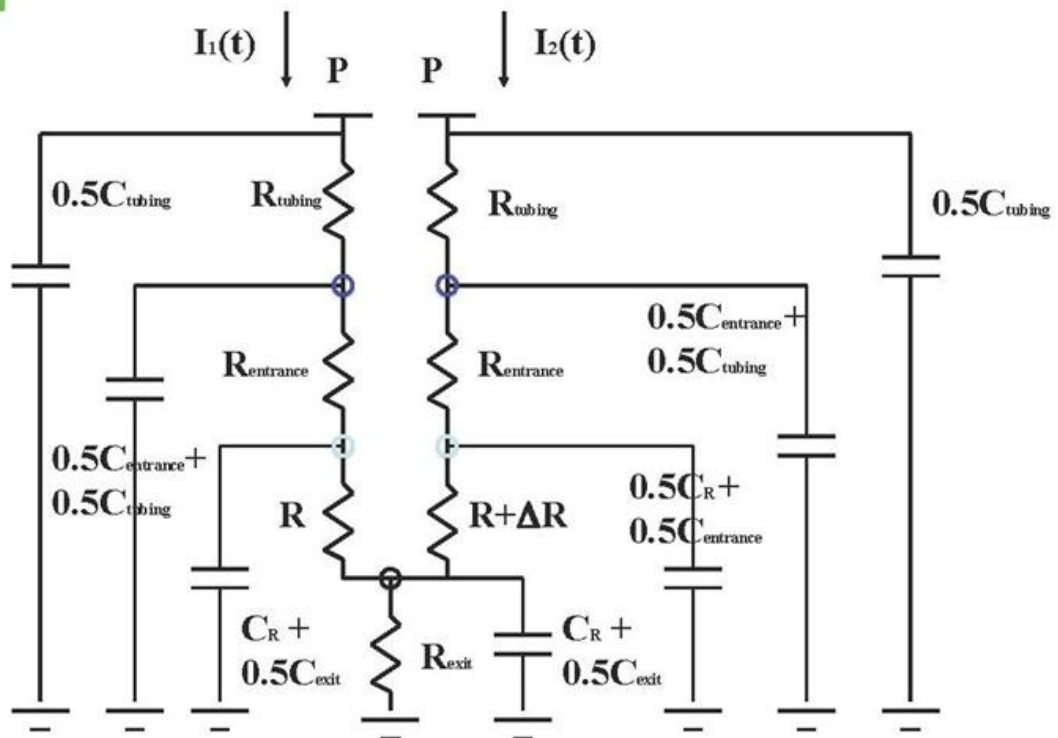


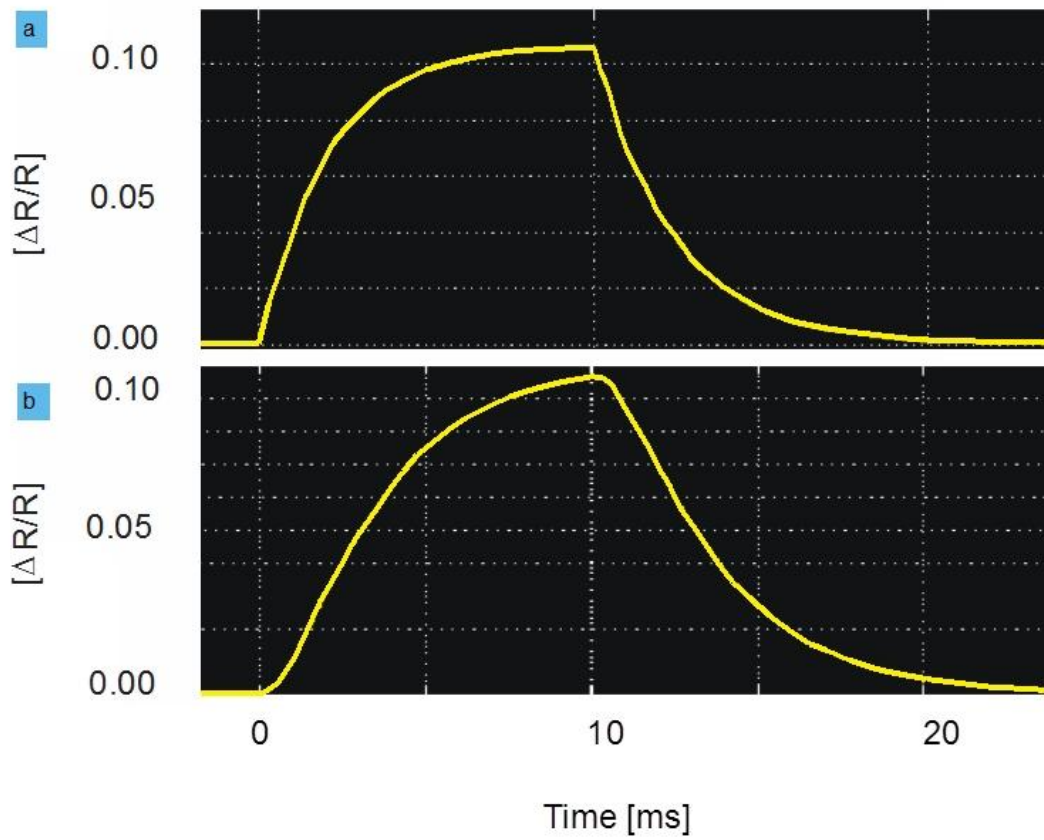
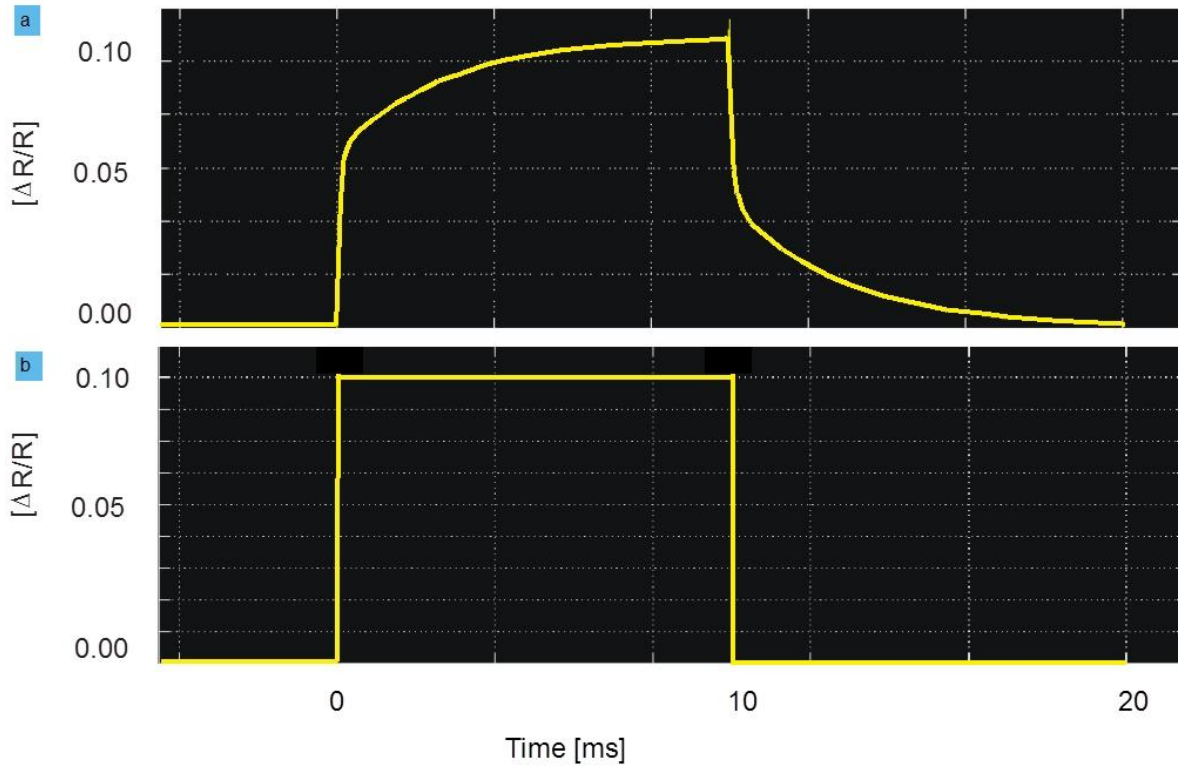


a

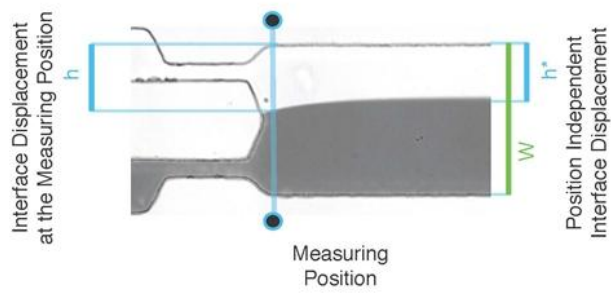


b





a



b

